This article has been accepted for publication in a future issue of this journal, but has not been fully edited. Content may change prior to final publication. Citation information: DOI 10.1109/TSTE.2019.2910726, IEEE Transactions on Sustainable Energy

Multi-Timescale Voltage Stability-Constrained Volt/VAR Optimization with Battery Storage System in Distribution Grids

Raheel Zafar, *Student Member, IEEE,* Jayashri Ravishankar, *Member, IEEE,*
John E. Fletcher, *Senior Member, IEEE,* and Hemanshu R. Pota, *Member, IEEE*

***Abstract*—This paper proposes multi-timescale voltage stability-constrained volt/VAR optimization to improve the steady-state stability and security of smart distribution grids. It aims to coordinate the post-contingency slow-timescale corrective actions provided by on-load tap changer with fast-timescale corrective actions provided by photovoltaic inverters and battery energy storage system. This multi-timescale operation exploits the difference between short- and long-term emergency ratings of line flows and voltage magnitudes usually defined by utilities for contingency cases. Global optimum is achieved by formulating the problem as mixed-integer second-order cone program (MISOCP). To justify the investment in battery storage, the proper coordination between base case state-of-charge and storage dynamic reserve margin required for post-contingency corrective actions is performed. Also, the steady-state voltage stability margin is computed through detailed voltage stability analysis. Simulation results demonstrate the effectiveness of proposed multi-timescale corrective actions in maintaining the steady-state stability and security under contingency cases.**

***Index Terms*—Battery storage dynamic reserve margin, convex relaxation, distribution grids, multi-timescale corrective actions, voltage stability-constrained volt/VAR optimization.**

I. INTRODUCTION

VOLTAGE stability-constrained volt/VAR optimization (VSC-VVO) model ensures pre- and post-contingency steady-state voltage stability subject to security (e.g., line flow and voltage magnitude limits) and economic constraints [1]. The VSC-VVO model solves the traditional volt/VAR optimization (VVO) problem while accounting for voltage stability limits in base and contingency cases. The growing load demand, increasing distributed energy resources (DERs), and competitive energy market usually lead to the operation of modern distribution grids closer to their operational limits. The robustness of the VVO solution against voltage instability can only be ensured by considering stability constraints in stressed distribution grids [2], [3].

Battery energy storage system (BESS) can be used for various applications such as energy arbitrage, peak shaving, and providing the stabilization required for the integration of intermittent renewable sources [4]. The heavy investments in BESS for post-contingency corrective control actions might be justified only when the BESS is simultaneously used for other standard applications during base case. Several researches have exploited the fast response capability of BESS [5]-[10]. Reference [5] reduced the required fast-ramping expensive generation through BESS. In [6], the photovoltaic (PV)/battery system is introduced into a security-constrained unit commitment for transmission congestion management. Reference [7] employed the system generators and microgrids (incl. storage) to relieve post-contingency overflows. Only microgrids were used for corrective control and these were not coordinated with generation redispatch to provide multi-timescale corrective actions. By contrast, reference [8] implemented multi-timescale corrective control scheme to relieve post-contingency overloads. The bulk and distributed energy storage exploited the short-term emergency (STE) and long-term emergency (LTE) ratings of lines, respectively. Similarly, the BESS reduced the line flows below STE rating and then generation redispatch kept the line flows below LTE rating after contingency [9]. The BESS state-of-charge (SOC), which significantly influences the storage ability to provide post-contingency corrective actions, was not considered. Reference [10] bridged this gap by assuming pre-specified initial BESS state-of-charge for multi-timescale corrective actions. However, the proper coordination mechanism between base case state-of-charge (very important for standard applications like arbitrage) and the BESS reserve margin required for post-contingency corrective actions was not considered. Above literature [6]-[10] mainly considers the transmission congestion management task and ignores voltage instability issue, which is vital in stressed power grids.

Voltage stability-constrained volt/VAR optimization is a mixed-integer nonlinear programming (MINLP) problem. The nonconvex equality constraints and presence of discrete control variables make it an NP-hard problem. Voltage stability margin (VSM) may be indirectly approximated by several heuristic voltage stability indices that provide suboptimal solutions for computational gains. By contrast, optimization approach involving two sets of constraints (one for normal and other for critical condition) provides accurate and direct means to compute VSM [11]. Reference [12] proposed a statistical approximation procedure to calculate VSM. In [13], the VSM is directly computed using optimization approach for reactive power planning problem. Reference [14] reduced the index of proximity to steady-state voltage collapse using non-dominated sorting genetic algorithm (NSGA-II). Similarly, particle swarm optimization (PSO) improved the voltage stability levels of buses in distribution grids [15]. Although evolutionary algorithms (e.g., PSO and NSGA-II) are flexible, they may not find a global optimum and usually lack performance guarantees due to nonconvex VSC-VVO model. This model may be convexified and solved efficiently through convex relaxations. For radial networks, the convex relaxations are always exact and yield global optimum provided there are no upper bounds on loads (sufficient but not necessary

1949-3029 (c) 2018 IEEE. Personal use is permitted, but republication/redistribution requires IEEE permission. See http://www.ieee.org/publications_standards/publications/rights/index.html for more information.

This article has been accepted for publication in a future issue of this journal, but has not been fully edited. Content may change prior to final publication. Citation information: DOI 10.1109/TSTE.2019.2910726, IEEE Transactions on Sustainable Energy

condition) [16], [17]. Reference [18] achieved global optimum of security-constrained optimal power flow problem through semidefinite program. However, it only considered line capacity constraints and ignored voltage stability constraints. Reference [2] formulated second-order cone program to reduce generation cost in voltage stability-constrained optimal power flow (VSC-OPF) problem. Here, the voltage stability constraint was approximated by a second-order conic representable voltage stability index. However, the BESS was not incorporated and multi-timescale corrective actions were not considered.

The recent transition from passive to active distribution networks demands an evolution from offline to online optimization. Reference [19] formulated a linearized power system model to solve multistage VVO problem in (near) real time. In [20], the power quality is improved by real-time voltage regulation scheme involving smart inverters. Reference [21] solved an online optimization problem to ensure the feasible operation of distribution grids under forecasting uncertainties by proposing a reconciliation algorithm. Our work in [22] coordinated the operation of VVO equipment in the presence of uncertainties involved in the forecasting of PV output and load demand using stochastic programming. Note that the forecasting uncertainties have an impact on VVO performance, however, the effects of uncertainties on distribution grid operation are beyond the scope of this paper. A comprehensive survey of real-time optimal power flow can be found in [23].

Traditional VVO equipment such as on-load tap changers (OLTCs) and switched capacitors can transition relatively slow (in seconds to minutes) due to their mechanical nature while recent DERs' converters can transition very fast (in milliseconds) [22]. This situation essentially enables the multi-timescale post-contingency corrective actions as the OLTCs with slow response and DERs' converters with fast response are effective control devices to achieve steady-state voltage stability [24]. Huge literature has considered the coordinated control of OLTCs with battery storage in standard VVO model [25]-[27]. Reference [25] reduced losses by the centralized control of OLTCs and battery storage. Similarly, the coordinated control of OLTCs and storage reduced losses along with voltage profile improvement [26]. Reference [27] formulated mixed-integer second-order cone program (MISOCP) to minimize energy purchase cost by coordinating OLTCs with battery storage. Only fewer applications of multi-timescale VVO models coordinating traditional VVO equipment with battery storage can be found in the literature. In our previous work [22], we implemented multi-timescale coordinated control of OLTCs and battery storage to reduce losses and energy purchase cost under forecasting uncertainties. Slow and fast timescales were coordinated using two-stage stochastic programming. Here, we now consider VSC-VVO model incorporating multi-timescale post-contingency corrective actions. In [28], intra-hour voltage regulation was performed through storage by assuming separation in slow and fast timescales. However, stability constraints and contingency cases were not considered. Reference [29] reduced losses through capacitors and inverters operating on slow and fast timescales. Again, stability constraints and battery storage were ignored and multi-timescale corrective actions were not implemented.

The motivation behind this work is to suggest a novel multi-timescale VSC-VVO model that not only exploits the STE and LTE ratings of lines (similar to [8], [9], and [10]) but also takes advantage of different steady-state voltage magnitude ratings usually defined by utilities for base and contingency cases. It is very clear that existing literature has not considered the multi-timescale corrective actions provided by the coordinated control of OLTC and battery storage. This paper considers the post-contingency fast-timescale corrective actions provided by battery storage and PV inverters while OLTC provides post-contingency slow-timescale corrective actions. In contrast to linearized or DC power flow model in [5], [7], and [19], the focus of this paper is to achieve the global optimum of original MINLP model by formulating the problem as MISOCP. The proposed method offers several technical and economic benefits to distribution system operator and customers. These benefits include enhanced system reliability, improved system voltage profile, reduced line losses, and improved environment due to more DERs' integration. To justify the heavy investment in BESS, this paper introduces a proper coordination mechanism between base case state-of-charge (very important for standard applications like arbitrage) and the BESS reserve margin required for post-contingency corrective actions. Also, the detailed voltage stability analysis is performed to compute voltage stability margin.

II. MULTI-TIMESCALE CORRECTIVE CONTROL

This section presents a conceptual illustration of multi-timescale corrective control scheme through simulation. It also formulates a preventive-corrective VSC-VVO model.

A. Multi-timescale Corrective Control Framework

Utilities usually not only define various thermal limits (e.g., normal, STE, and LTE ratings) to avoid damage to power components but also specify several steady-state voltage levels. EirGrid system maintains 0.95-1.1 pu in base case and 0.9-1.12 pu in N-1 contingency cases [30]. Similarly, Western Power Australia allows $\pm 6\%$ during normal conditions and $\pm 10\%$ during emergency conditions in distribution grids [31]. Fig. 1 shows a three-node radial system for simulation purpose. Fig. 2 provides the explanation of time axis used in this paper. The contingency occurs at instant t_1 and fast-timescale corrective actions provided by BESS are applied at instant t_2. The ramping of slow-timescale corrective actions provided by OLTC is initiated at instant t_{ramp} and concluded at instant t_3. The STE rating is considered from t_2 to t_3 while LTE rating (usually same as normal rating) is considered from t_3 onwards.

The effectiveness of multi-timescale corrective actions in mitigating line overflow and voltage limit violations is demonstrated by simulation. Fig. 3(a) shows that both line flow and voltage exceed STE limits when PV inverter contingency is realized at instant t_1. The increase in line flow F_{12} due to constant power load results in greater voltage drop across line and transformer impedances. Fig. 3(b) shows that BESS active power P_{BESS} increases at instant t_2 to bring F_{12} within limit and reduces voltage drop. Also, the BESS reactive power Q_{BESS} provides voltage support to bring V_2 back to voltage STE rating. The tap movement concludes at instant t_3 and both line flow and voltage are within LTE limits.

1949-3029 (c) 2018 IEEE. Personal use is permitted, but republication/redistribution requires IEEE permission. See http://www.ieee.org/publications_standards/publications/rights/index.html for more information.

This article has been accepted for publication in a future issue of this journal, but has not been fully edited. Content may change prior to final publication. Citation information: DOI 10.1109/TSTE.2019.2910726, IEEE Transactions on Sustainable Energy

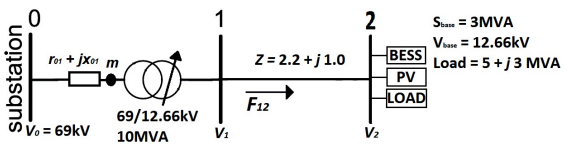

Fig. 1. Three-node radial system used for simulation.

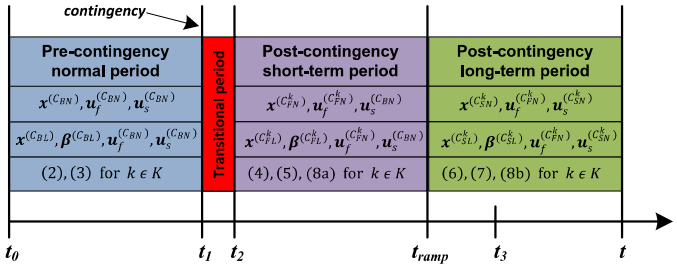

Fig. 2. Illustration of proposed multi-timescale VSC-VVO framework.

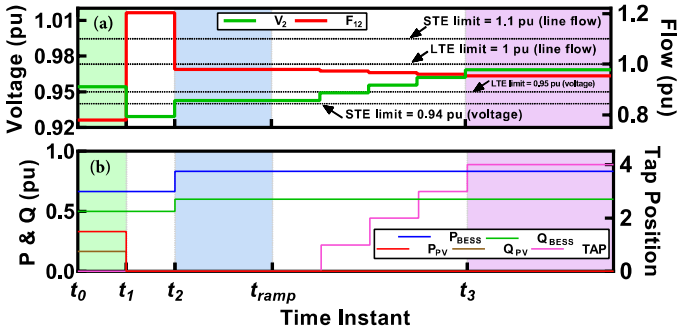

Fig. 3. (a) Voltage and line flow. (b) Power injections and tap position.

B. Multi-timescale Preventive-corrective VSC-VVO Model

This subsection integrates the voltage stability constraints into the formulation given in [9]. This paper computes voltage stability margin through optimization approach involving two sets of constraints (one for normal condition and other for critical condition). Here, steady-state VSM is quantified in terms of MW distance from the operating point to critical point or point of voltage instability (PVI) [3].

Define $C := \{C_{BN}, C_{BL}, C_{FN}^1, ..., C_{FN}^{N_C}, C_{FL}^1, ..., C_{FL}^{N_C}, C_{SN}^1, ..., C_{SN}^{N_C}, C_{SL}^1, ..., C_{SL}^{N_C}\}$ as the set of all pre- and post-contingency cases and $K := \{1, 2, ..., N_C\}$ as the set of N_C (positive integer) contingencies. The C_{BN} and C_{BL} denote base case scenarios at normal and critical conditions, respectively. For contingency number $k \in K$, the C_{FN}^k and C_{FL}^k represent the kth fast-timescale contingency cases at normal and critical states, respectively. Similarly, the kth slow-timescale contingency cases at normal and critical conditions are described by C_{SN}^k and C_{SL}^k, respectively. The multi-timescale preventive-corrective VSC-VVO model can be formulated as:

$$\text{minimize} \quad \sum_{c \in C} \sigma^{(c)} \, f_{(c)}(x^{(c)}, u_f^{(c)}, u_s^{(c)}) \tag{1}$$

subject to (2)-(8)

$$g_{(C_{BN})}(x^{(C_{BN})}, u_f^{(C_{BN})}, u_s^{(C_{BN})}) = 0 \tag{2a}$$

$$h_{(C_{BN})}(x^{(C_{BN})}, u_f^{(C_{BN})}, u_s^{(C_{BN})}) \le h_{max}^{(C_{BN})} \tag{2b}$$

$$g_{(C_{BL})}(x^{(C_{BL})}, u_f^{(C_{BN})}, u_s^{(C_{BN})}) = 0 \tag{3a}$$

$$h_{(C_{BL})}(x^{(C_{BL})}, \beta^{(C_{BL})}, u_f^{(C_{BN})}, u_s^{(C_{BN})}) \le h_{max}^{(C_{BL})} \tag{3b}$$

$$g_{(C_{FN}^k)}(x^{(C_{FN}^k)}, u_f^{(C_{FN}^k)}, u_s^{(C_{BN})}) = 0 \tag{4a}$$

$$h_{(C_{FN}^k)}(x^{(C_{FN}^k)}, u_f^{(C_{FN}^k)}, u_s^{(C_{BN})}) \le h_{max}^{(C_{FN}^k)} \tag{4b}$$

$$g_{(C_{FL}^k)}(x^{(C_{FL}^k)}, u_f^{(C_{FN}^k)}, u_s^{(C_{BN})}) = 0 \tag{5a}$$

$$h_{(C_{FL}^k)}(x^{(C_{FL}^k)}, \beta^{(C_{FL}^k)}, u_f^{(C_{FN}^k)}, u_s^{(C_{BN})}) \le h_{max}^{(C_{FL}^k)} \tag{5b}$$

$$g_{(C_{SN}^k)}(x^{(C_{SN}^k)}, u_f^{(C_{FN}^k)}, u_s^{(C_{SN}^k)}) = 0 \tag{6a}$$

$$h_{(C_{SN}^k)}(x^{(C_{SN}^k)}, u_f^{(C_{FN}^k)}, u_s^{(C_{SN}^k)}) \le h_{max}^{(C_{SN}^k)} \tag{6b}$$

$$g_{(C_{SL}^k)}(x^{(C_{SL}^k)}, u_f^{(C_{FN}^k)}, u_s^{(C_{SN}^k)}) = 0 \tag{7a}$$

$$h_{(C_{SL}^k)}(x^{(C_{SL}^k)}, \beta^{(C_{SL}^k)}, u_f^{(C_{FN}^k)}, u_s^{(C_{SN}^k)}) \le h_{max}^{(C_{SL}^k)} \tag{7b}$$

$$|u_f^{(C_{FN}^k)} - u_f^{(C_{BN})}| \le \Delta u_{f;max}^{(C_{FN}^k)} \tag{8a}$$

$$|u_s^{(C_{SN}^k)} - u_s^{(C_{BN})}| \le \Delta u_{s;max}^{(C_{SN}^k)} \tag{8b}$$

for every $c \in C$ and $k \in K$. The $u_f^{(c)}$ denotes fast-timescale control variables (e.g., BESS active/reactive power and PV inverter reactive power output) and $u_s^{(c)}$ defines slow-timescale controls (e.g., OLTCs' tap positions) for scenario c. The $x^{(c)}$ describes state variables and $\sigma^{(c)}$ refers to probability of pre- and post-contingency scenarios. The equality constraint set [(2a), (3a), (4a), (5a), (6a), (7a)] mainly describes load flow equations. Equation (2a) also includes BESS state-of-charge. The inequality constraint set [(2b), (4b), (6b)] includes physical limits of components and operational limits of distribution grids at normal condition. In contrast, the inequality constraint set [(3b), (5b), (7b)] mainly includes voltage stability constraints involving load multiplier β at critical condition. Depending on the context, the h_{max} denotes the normal, STE, or LTE rating of power component. Note that STE rating is considered from t_2 to t_3 so constraints associated with ramping period are unnecessary and post-contingency slow-timescale constraints are defined only at instant t_3. The applicability of these constraints and variables are summarized in Fig. 2. Detailed explanation of constraints is included in the next section.

Coupling constraint (8) limits the movements of control variables between base and post-contingency cases. This paper assumes unrestricted variations of control variables ($\Delta u_{f;max} = \Delta u_{s;max} = +\infty$). If post-contingency constraints are violated then VSC-VVO model first takes the corrective measures to ensure security and stability. This is due to small cost of corrective actions as the contingencies occur rarely and do not last for long time period. The preventive measures are taken only if necessary as the preventive actions $(u_f^{(C_{BN})}, u_s^{(C_{BN})})$ may operate the system away from optimal point for long period irrespective of contingency event. This makes preventive actions costlier than corrective actions [32].

III. PROBLEM FORMULATION

This section converts the original MINLP problem to MISOCP model to achieve global optimum. Proper coordination mechanism for base case state-of-charge and BESS dynamic reserve margin required for corrective actions is presented.

A. MINLP Formulation for Multi-timescale VSC-VVO Model

Fig. 4 shows a radial distribution network with set of buses $\mathcal{N} := \{0, 1, 2, ..., N_{BUS}\}$ and its load flow equations can be represented by DistFlow branch equations [34]. Let $p_{i,t}$ and $q_{i,t}$ be net active and reactive power injections at bus i, respectively. Define $P_{ij,t}$, $Q_{ij,t}$, and $L_{ij,t}$ as the active power, reactive power, and squared current flows from bus i to j, respectively. The voltage magnitude and squared voltage at bus i

1949-3029 (c) 2018 IEEE. Personal use is permitted, but republication/redistribution requires IEEE permission. See http://www.ieee.org/publications_standards/publications/rights/index.html for more information.

This article has been accepted for publication in a future issue of this journal, but has not been fully edited. Content may change prior to final publication. Citation information: DOI 10.1109/TSTE.2019.2910726, IEEE Transactions on Sustainable Energy

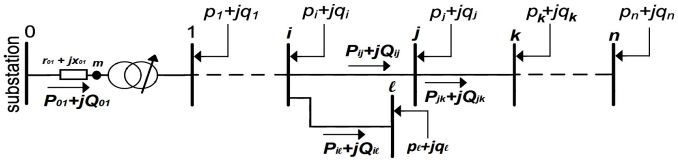

Fig. 4. Single line diagram of radial distribution system [22], [33].

are denoted by $v_{i,t}$ and $U_{i,t}$, respectively. The objective of proposed multi-timescale VSC-VVO model is to minimize losses (9) while ensuring voltage stability and security constraints. The mixed-integer nonlinear programming model is given by

$$\text{minimize} \quad \sum_{c\in C}\sum_{t\in\mathcal{T}}\sum_{i\in\mathcal{N}} \sigma_t^{(c)}\ p_{i,t}^{(c)} \tag{9}$$

subject to (10)-(24)

$$P_{jk,t}^{(c)} = P_{ij,t}^{(c)} - r_{ij}L_{ij,t}^{(c)} + p_{j,t}^{(c)} \tag{10}$$

$$Q_{jk,t}^{(c)} = Q_{ij,t}^{(c)} - x_{ij}L_{ij,t}^{(c)} + q_{j,t}^{(c)} \tag{11}$$

$$U_{j,t}^{(c)} = U_{i,t}^{(c)} - 2(r_{ij}P_{ij,t}^{(c)} + x_{ij}Q_{ij,t}^{(c)}) + (r_{ij}^2 + x_{ij}^2)L_{ij,t}^{(c)} \tag{12}$$

$$U_{m,t}^{(c)} = U_{0,t}^{(c)} - 2(r_{01}P_{01,t}^{(c)} + x_{01}Q_{01,t}^{(c)}) + (r_{01}^2 + x_{01}^2)L_{01,t}^{(c)} \tag{13a}$$

$$U_{1,t}^{(c)} = (TAP_t^{(c)})^2 \times U_{m,t}^{(c)} \tag{13b}$$

$$TAP_t^{(c)} = TAP^{min} + tap_t^{(c)}\ \Delta TAP \tag{13c}$$

$$\Delta TAP = (TAP^{max} - TAP^{min})/N_{TAP} \tag{13d}$$

$$L_{ij,t}^{(c)} = \{(P_{ij,t}^{(c)})^2 + (Q_{ij,t}^{(c)})^2\}/U_{i,t}^{(c)} \tag{14}$$

$$p_{j,t}^{(c)} = p_{j,t}^{g\ (c)} + p_{j,t}^{DIS\ (c)} - p_{j,t}^{CHA\ (c)} - p_{j,t}^{d\ (c)} \tag{15}$$

$$q_{j,t}^{(c)} = q_{j,t}^{g\ (c)} + q_{j,t}^{cap\ (c)} + q_{j,t}^{BESS\ (c)} - q_{j,t}^{d\ (c)} \tag{16}$$

$$0 \le tap_t^{(c)} \le N_{TAP} \tag{17}$$

$$(v_{i;min}^{(c)})^2 \le (U_{i,t}^{(c)} = |v_{i,t}^{(c)}|^2) \le (v_{i;max}^{(c)})^2 \tag{18}$$

$$(p_{i,t}^{g\ (c)})^2 + (q_{i,t}^{g\ (c)})^2 \le (S_{i,PV;max}^{(c)})^2 \tag{19}$$

$$(P_{ij,t}^{(c)})^2 + (Q_{ij,t}^{(c)})^2 \le (S_{ij,line;max}^{(c)})^2 \tag{20}$$

for every $c \in C$ and $t \in \mathcal{T}$, where $\mathcal{T}$ is the set of time instants up to T_N. The r_{ij} and x_{ij} denote resistance and reactance of branch (i,j), respectively. The tap_t is tap position of OLTC, N_{TAP} refers to total number of taps, and $q_{i,t}^{cap}$ describes capacitor reactive power. The PV active and reactive powers are denoted by $p_{i,t}^g$ and $q_{i,t}^g$ while active and reactive load demands are indicated by $p_{i,t}^d$ and $q_{i,t}^d$. The BESS charging, discharging, and reactive powers are denoted by $p_{i,t}^{CHA}$, $p_{i,t}^{DIS}$, and $q_{i,t}^{BESS}$, respectively. The apparent power ratings of PV inverter and line (i,j) are indicated by $S_{i,PV;max}$ and $S_{ij,line;max}$.

Eqs. (10)-(12) describe DistFlow branch equations for lines while (13) indicates DistFlow equations for substation OLTC. Eqs. (15)-(16) assume plus/minus signs for power injection/extraction. When certain power equipment is not installed at a bus, corresponding entry will become zero in (15)-(16). Section III-B includes detailed BESS model. The limits on taps, voltages, and apparent powers are indicated by (17)-(20).

Multi-timescale corrective actions are realized by (21)-(22). The control setpoints at critical condition are assumed to be same as setpoints at normal condition for computing voltage stability margin. The slow-timescale controls provided by OLTCs remain same between base and fast-timescale contingency cases. This exhibits preventive behavior (21a) during post-contingency short-term period and corrective behavior (21b) during post-contingency long-term period. By contrast, equation (22b) shows that fast-timescale corrective actions provided by PV units (also by battery storage) are applied during post-contingency short-term period.

$$tap_t^{(C_{BN})} = tap_t^{(C_{BL})} = tap_t^{(C_{FN}^k)} = tap_t^{(C_{FL}^k)} \tag{21a}$$

$$tap_t^{(C_{SN}^k)} = tap_t^{(C_{SL}^k)} \tag{21b}$$

$$q_{i,t}^{g\ (C_{BN})} = q_{i,t}^{g\ (C_{BL})} \tag{22a}$$

$$q_{i,t}^{g\ (C_{FN}^k)} = q_{i,t}^{g\ (C_{FL}^k)} = q_{i,t}^{g\ (C_{SN}^k)} = q_{i,t}^{g\ (C_{SL}^k)} \tag{22b}$$

Consider $c \in \{C_{BL}, C_{FL}^k, C_{SL}^k\}$ and $k \in K$. Let pf_i be load power factor and VSM_{target} be the pre-specified VSM target. The difference in the "normal" and "critical" states' total MW load is kept apart by a minimum VSM_{target} [12]. Note that voltage stability margin constraints (23) [13] are included only at critical states. This paper assumes proportional increase of loads (23a) and maintains constant load power factors (23b) at critical states. Other loading directions can be considered based on the expected pattern of increase from the initial loads.

$$p_{i,t}^{d\ (c)} = \beta^{(c)} \times p_{i,t}^{d\ (C_{BN})} \tag{23a}$$

$$\frac{p_{i,t}^{d\ (c)}}{q_{i,t}^{d\ (c)}} = \frac{pf_i}{(1-pf_i^2)^{1/2}} = H_i \tag{23b}$$

$$\beta^{(c)} \ge 1/(1 - VSM_{target}^{(c)}) \tag{23c}$$

IEEE task force on volt/VAR control mentioned PV inverter shutdown event [35]. This paper assumes all N-1 PV inverter outage contingencies. Line outages are not considered because any fault in the grid could result in islanding and disconnection of loads. The outage of PV unit at bus i can be modeled as

$$p_{i,t}^{g\ (c)} = q_{i,t}^{g\ (c)} = S_{i,PV;max}^{(c)} = 0 \tag{24}$$

The MINLP model (9)-(24) for multi-timescale VSC-VVO is nonconvex due to quadratic equalities in (13b) and (14).

B. Battery Energy Storage System

The battery storage model is given by (25) [17] with $c \in C$. The dynamic equality constraint (25a) is convex and links adjacent intervals of duration Δt. Equal initial and final state-of-charge are ensured by (25c). Eqs. (25b)-(25e) are linear constraints while (25f) is convex quadratic inequality constraint.

$$SOC_{i,t}^{(C_{BN})} = \alpha_i\ SOC_{i,t-1}^{(C_{BN})} + \Delta t\ (\eta_i^{CHA}\ p_{i,t}^{CHA(C_{BN})} - p_{i,t}^{DIS(C_{BN})}/\eta_i^{DIS}) \tag{25a}$$

$$0 \le SOC_{i,t}^{(C_{BN})} \le SOC_{i;max} \tag{25b}$$

$$SOC_{i,T_N}^{(C_{BN})} = SOC_{i,0}^{(C_{BN})} \tag{25c}$$

$$0 \le p_{i,t}^{CHA\ (c)} \le - PCHA_{i;max}^{(c)}\ \xi_{i,t}^{(c)} \tag{25d}$$

$$0 \le p_{i,t}^{DIS\ (c)} \le PDIS_{i;max}^{(c)}\ (1 - \xi_{i,t}^{(c)}) \tag{25e}$$

$$(p_{i,t}^{DIS(c)} - p_{i,t}^{CHA(c)})^2 + (q_{i,t}^{BESS(c)})^2 \le (S_{i,BESS;max}^{(c)})^2 \tag{25f}$$

where $SOC_{i,t}$ is the storage state-of-charge at instant t and $SOC_{i;max}$ is energy capacity rating. The α_i, η_i^{CHA}, and η_i^{DIS} denote self-discharge, charging, and discharging efficiencies, respectively. The BESS charging, discharging, and apparent power ratings are respectively defined by $PCHA_{i;max}$, $PDIS_{i;max}$, and $S_{i,BESS;max}$. The binary variable $\xi_{i,t}$ prevents simultaneous charging and discharging of storage.

1949-3029 (c) 2018 IEEE. Personal use is permitted, but republication/redistribution requires IEEE permission. See http://www.ieee.org/publications_standards/publications/rights/index.html for more information.

This article has been accepted for publication in a future issue of this journal, but has not been fully edited. Content may change prior to final publication. Citation information: DOI 10.1109/TSTE.2019.2910726, IEEE Transactions on Sustainable Energy

Define $C^k := \{C^k_{FN}, C^k_{FL}, C^k_{SN}, C^k_{SL}\}$ as the set of kth post-contingency scenario, where $C^k \subseteq C$, $c \in C^k$, and $k \in K$. This paper introduces a proper coordination mechanism between base case state-of-charge (very important for standard applications like arbitrage) and the BESS reserve margin required for post-contingency corrective actions by replacing (25b) with (26). The BESS reserve margin includes the amount of energy that must be delivered or stored to guard against all the contingencies. It also includes the BESS contribution towards the reduction of post-contingency cost function weighted by contingency probabilities. Note that maximum of convex functions is convex so it can be seamlessly integrated into inequality constraint without compromising its convexity.

$$[\{max(p^{DIS\ (c)}_{i,t})/\eta^{DIS}_i\} \times \Delta t] \leq SOC^{(C_{BN})}_{i,t} \tag{26a}$$

$$[\eta^{CHA}_i \times max(p^{CHA\ (c)}_{i,t}) \times \Delta t] + SOC^{(C_{BN})}_{i,t} \leq SOC_{i,max} \tag{26b}$$

Previous work such as [9] suggested similar reserve margin constraints (w/o η^{CHA}_i and η^{DIS}_i) but didn't coordinate them with BESS state-of-charge. By contrast, our dynamic approach is less conservative and more economical. Note that storage systems are usually seen as active power sources and additional reactive power capability comes from power electronics used to connect them to distribution grids. The constraints (19) and (25f) governing reactive power capability of PV units and storage are sufficient for the purpose of VSC-VVO model [17].

C. MISOCP Formulation of Multi-timescale VSC-VVO Model

This subsection presents MISOCP formulation for multi-timescale VSC-VVO model. Reference [33] used binary expansion scheme to replace (17) by (27a) and big-M method to transform nonconvex constraint (13b) into mixed-integer linear expressions. Consider $c \in C$ and substituting new variables $m^{(c)}_t = TAP^{(c)}_t\ U^{(c)}_{m,t}$, $x^{(c)}_{n,t} = \lambda^{(c)}_{n,t}\ U^{(c)}_{m,t}$, and $y^{(c)}_{n,t} = \lambda^{(c)}_{n,t}\ m^{(c)}_t$ in (13b) and (13c) would result in (27b)-(27g) via big-M method.

$$\sum\nolimits_{n=0}^{N_{BIN}} 2^n \lambda^{(c)}_{n,t} \leq N_{TAP} \tag{27a}$$

$$m^{(c)}_t = TAP^{min} U^{(c)}_{m,t} + \Delta TAP \sum\nolimits_{n=0}^{N_{BIN}} 2^n x^{(c)}_{n,t} \tag{27b}$$

$$0 \leq U^{(c)}_{m,t} - x^{(c)}_{n,t} \leq (1 - \lambda^{(c)}_{n,t}) M_1 \tag{27c}$$

$$0 \leq x^{(c)}_{n,t} \leq \lambda^{(c)}_{n,t} M_1 \tag{27d}$$

$$U^{(c)}_{1,t} = TAP^{min} m^{(c)}_t + \Delta TAP \sum\nolimits_{n=0}^{N_{BIN}} 2^n y^{(c)}_{n,t} \tag{27e}$$

$$0 \leq m^{(c)}_t - y^{(c)}_{n,t} \leq (1 - \lambda^{(c)}_{n,t}) M_2 \tag{27f}$$

$$0 \leq y^{(c)}_{n,t} \leq \lambda^{(c)}_{n,t} M_2 \tag{27g}$$

where $\lambda_{n,t}$ is a binary variable, N_{BIN} denotes binary expansion length, M_1 and M_2 are big-M method constants.

Exact linearized OLTC model (27) [33] has replaced nonconvex constraint (13b). Reference [16] describes two relaxation steps to convexify (14). Angle relaxation step results in (12) and (14) by taking squared complex magnitudes. Applying second-order cone relaxation step on (14) gives

$$L^{(c)}_{ij,t} \geq \{(P^{(c)}_{ij,t})^2 + (Q^{(c)}_{ij,t})^2\}/U^{(c)}_{i,t} \tag{28}$$

MISOCP based multi-timescale VSC-VVO model is given by

$$\text{minimize} \quad \sum_{c \in C} \sum_{t \in \mathcal{T}} \sum_{i \in \mathcal{N}} \sigma^{(c)}_t\ p^{(c)}_{i,t} \tag{29}$$

subject to (10)-(13a), (13d), (15), (16), (18)-(25a), (25c)-(28).

The global optimum would attain the equality of (28) if MISOCP relaxation is exact. For radial networks, the convex relaxations are always exact and yield global optimum provided there are no upper bounds on loads (sufficient but not necessary condition) [16], [17]. The proofs relevant to the exactness of convex relaxation for radial grids are given by ([16], Theorems 1 and 4) and ([17], Theorem 3.1). Exact relaxation results in feasible (hence globally optimal) solution while inexact relaxation yields infeasible solution that only gives a lower bound on true optima [17]. Note that the simulation studies in Section V-A and V-B always resulted in global optimum by attaining equality of (28).

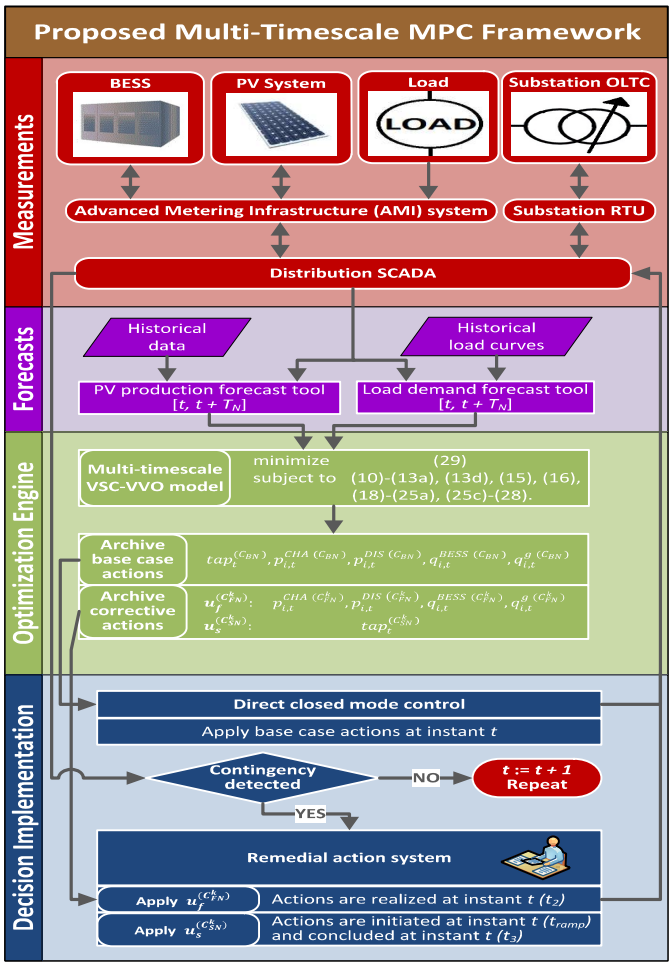

Fig. 5. Proposed multi-timescale operational framework.

IV. MULTI-TIMESCALE MPC FRAMEWORK

Fig. 5 shows the proposed multi-timescale operational framework based on model predictive control (MPC) algorithm. The advanced metering infrastructure (AMI) system receives the equipment measurements and status while sends the control signals to battery storage and PV inverters. Similarly, the substation remote terminal unit (RTU) monitor and control the tap position of OLTC. The proposed multi-timescale MPC framework is dictated by the distribution management system (DMS), which is consistent with [19]. Here, the DMS software inventory includes distribution SCADA, PV production forecast tool, demand-forecasting tool, VSC-VVO optimization engine, and remedial action system (RAS). Also, the details about the AMI-DMS integration can be found in [36].

The demand and PV output profiles are assumed to be forecasted based on historical data and actual measurements

1949-3029 (c) 2018 IEEE. Personal use is permitted, but republication/redistribution requires IEEE permission. See http://www.ieee.org/publications_standards/publications/rights/index.html for more information.

This article has been accepted for publication in a future issue of this journal, but has not been fully edited. Content may change prior to final publication. Citation information: DOI 10.1109/TSTE.2019.2910726, IEEE Transactions on Sustainable Energy

at instant $t-1$. These forecasted profiles are used by VSC-VVO optimization engine to compute the base case and post-contingency corrective set-points for the entire prediction horizon between t and $t+T_N$. The proposed MPC framework only implements the first decision variables and the same procedure is repeated for the next prediction horizon. Note that the proposed control framework can be seamlessly integrated into the day-ahead and hour-ahead energy markets.

The localized control of PV inverters and OLTC equipped with line drop compensator (LDC) could result in hunting phenomenon among equipment that may interfere with network control. Also, the localized control methods cause increased tap operation of OLTC under high PV penetration [25]. By contrast, the proposed MPC framework based on centralized approach avoids hunting phenomenon and mechanical wear and tear due to the frequent switching of OLTC. The proposed centralized implementation would be relatively fast as it does not introduce intentional time delay between 30 seconds and 5 minutes to prevent hunting among equipment. The tap changer equipped with LDC experiences unintended automatic raise operation due to long-term voltage instability issue [24]. The proposed approach enables the OLTC blocking operation to avoid the negative actions of OLTC in critical conditions.

V. SIMULATION RESULTS AND ANALYSIS

The proposed multi-timescale voltage stability-constrained volt/VAR optimization is examined on modified IEEE 33-bus feeder [34] as shown in Fig. 6. The BESS and PV units provide post-contingency fast-timescale corrective actions while OLTC provides post-contingency slow-timescale corrective actions. Assume that substation voltage v_0 is 1.0 pu and OLTC has $\pm 10\%$ tap range and 32 tap positions (i.e., tap=[-16,16]). Previous literature such as [8]-[10] has considered only single operating point. This paper assumes PV generation profile from NREL [37] and hourly load profile from SCE [38] on 25th April, 2018 as the computation of dynamic reserve margin of battery storage demands multi-period optimization. The loading factor in Fig. 7 is the percentage value of initial operating point and highlighted portion is the period of interest. All N-1 PV inverter outage contingencies are considered and corresponding probabilities are indicated in Table I. Here, mean time to failure of each PV inverter is assumed to be 800h (see [39] for detailed probability calculations). GAMS/CPLEX [40] is used to solve MISOCP problem on ordinary PC.

A. VSC-VVO Model Operating in Fully Corrective Mode

This subsection explores the situation when multi-timescale VSC-VVO model operates in fully corrective mode. Initial operating point load is 3.715 MW and 2.3 MVAR. Assume that each shunt capacitor has 30 kVAR rating. The BESS installed at bus 33 is assumed to have a capacity of 1.1 MVA/5 MWh. Also, the PV inverters each with the rating of 550 kVA are installed at bus 11, 12, 22, and 29. The proposed model maintains 0.95-1.05 pu in normal condition and 0.93-1.07 pu in STE condition. The STE branch flow limit (1.56 MVA) is assumed to be 1.2 times larger than normal limit (1.3 MVA). The LTE ratings for both voltage and line flow are assumed to be equal to normal ratings. The voltage magnitudes and line flow limits are unbounded at critical condition. Other operational range can be considered based on system's data.

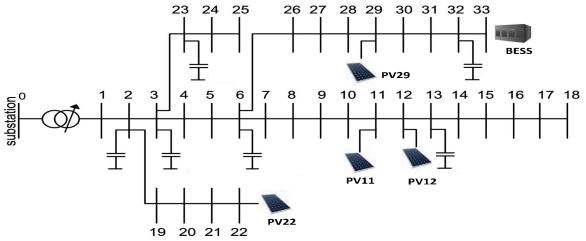

Fig. 6. IEEE 33-bus test feeder [22], [34].

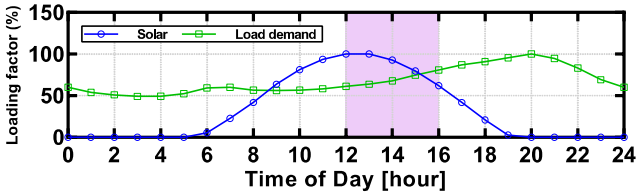

Fig. 7. Load demand and solar generation profiles.

TABLE I
CONTINGENCY SCENARIOS AND PROBABILITIES

Scenario	$\sigma_t^{(C_{BN})}$	$\sigma_{12}^{(C^k)}$	$\sigma_{13}^{(C^k)}$	$\sigma_{14}^{(C^k)}$	$\sigma_{15}^{(C^k)}$
Probability (%)	98.0198	0.1230	0.1229	0.1227	0.1226

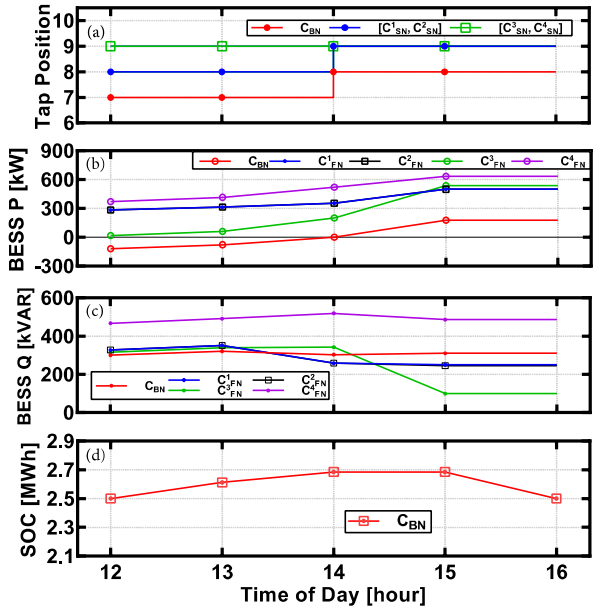

Fig. 8. (a) OLTC tap position. (b) Battery storage active power flow. (c) Battery storage reactive power flow. (d) Battery storage state-of-charge.

Fig. 8(a) shows that tap position is high between 14:00-15:00 (case C_{BN}) due to increased load demand and reduced solar generation. Fig. 8(b) shows that the battery storage is charging between 12:00-13:00 (case C_{BN}) when load demand is low and PV output is high. By contrast, the BESS reduces power losses by discharging at instant 15:00 (case C_{BN}) when demand is highest and PV output is lowest. Fig. 8(c) depicts the voltage support provided by BESS reactive power injections for all pre- and post-contingency cases. Note that multi-timescale corrective actions are (almost) same for contingencies C^1 and C^2 due to PV11 and PV12 being installed at adjacent buses. The contingencies C^3 and C^4 denote PV22 and PV29 outages. Fig. 8(d) shows that BESS state-of-charge meets the constraint (25c) of same initial and final values.

Fig. 9(a) shows the substation active and reactive power flow for base case. Active power flow is maximum at instant 15:00

1949-3029 (c) 2018 IEEE. Personal use is permitted, but republication/redistribution requires IEEE permission. See http://www.ieee.org/publications_standards/publications/rights/index.html for more information.

This article has been accepted for publication in a future issue of this journal, but has not been fully edited. Content may change prior to final publication. Citation information: DOI 10.1109/TSTE.2019.2910726, IEEE Transactions on Sustainable Energy

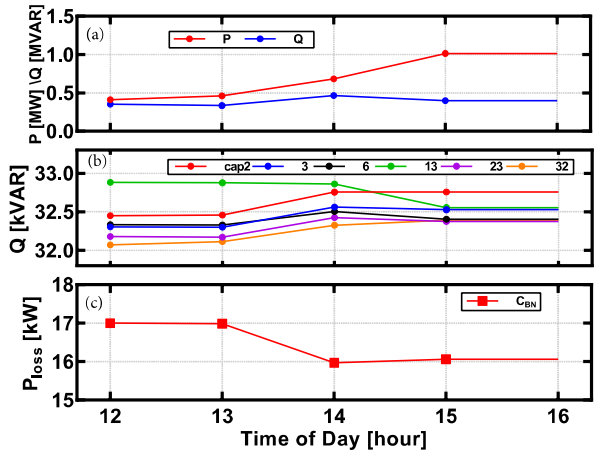

Fig. 9. Base case. (a) Substation active and reactive power flow. (b) Shunt capacitors reactive power injections. (c) Distribution losses.

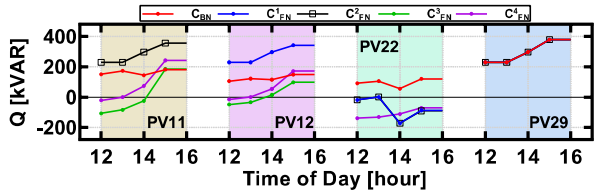

Fig. 10. PV inverters' reactive power output.

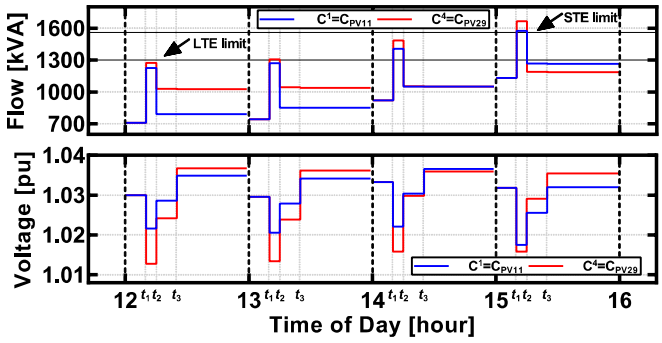

Fig. 11. Simulation. (a) Maximum line flow. (b) Minimum voltage profile.

due to high load demand and low PV generation. Fig. 9(b) depicts the dependence of capacitors' reactive power injections on voltage magnitudes at the respective buses. Fig. 9(c) shows the total losses including storage charging and discharging losses (η^{CHA}=η^{DIS}=0.95). Reactive power support provided by PV units to guard against all contingencies is shown in Fig. 10. Different reactive power output indicates the reliance of corrective actions on PV units' locations.

Fig. 11 includes the solutions provided by optimization model (for normal, short-term, and long-term periods) and OpenDSS load flow package (for transitional period). Here, we assume the time-axis (i.e., t_1, t_2, t_3) definitions as described in Section II. Fig. 11(a) shows the violation of line flow STE limit during transitional period at instant 15:00 (t_1). The corrective actions then keep the post-contingency line flows within limits. Similarly, the voltage decreases upon the occurrence of contingency at instant t_1 in Fig. 11(b). The multi-timescale corrective actions then improve the minimum voltage profile to reduce post-contingency losses.

Fig. 12 demonstrates the proper coordination between base case state-of-charge and BESS dynamic reserve margin required for post-contingency corrective actions. These corrective actions contribute towards the mitigation of constraint violations and reduction of cost function (e.g., losses). The proper coordination mechanism is provided by constraint (26). Here, the corrective actions are provided in the form of discharges with minimum overall reserve margin for contingency C^3 and maximum overall reserve margin for contingency C^4.

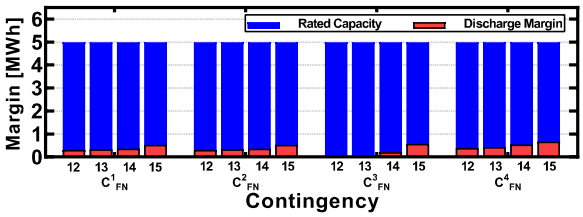

Fig. 12. Battery storage dynamic reserve margin for corrective actions.

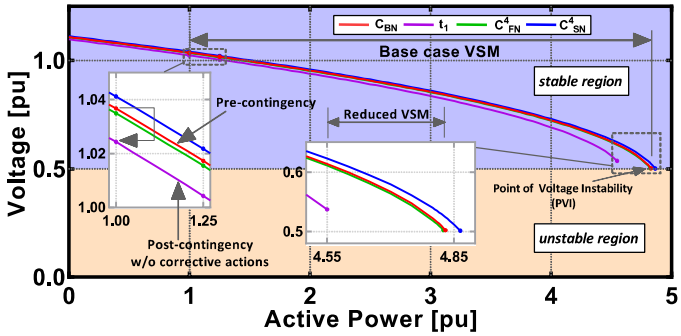

Fig. 13. P-V curves for steady-state voltage stability analysis.

Fig. 13 shows the P-V curves computed for incremental load increase with fixed control variable settings using quasi-dynamic simulations in OpenDSS. The P-V curves are plotted at instant 15:00 and bus 18 is assumed to be a representative bus due to minimum voltage magnitude. Any other representative bus can be considered. The 20% VSM target requires load multiplier β to be at least 1.25 pu as per (23c). Note that operating point at critical state can be anywhere between minimum β value and point of voltage instability. Here, the critical operating point is maintained at 1.25 pu due to the nature of post-contingency cost function (i.e., loss reduction). The VSM is reduced from 3.83 pu (case C_{BN}) to 3.55 pu (instant t_1) upon the introduction of C^4 contingency. Multi-timescale corrective actions then increase the VSM to 3.865 pu. Only corrective measures were taken to ensure security and stability as both VVO and VSC-VVO models resulted in exactly same overall loss of 66.02 kW. Also, the load flow solution failed to converge beyond nose point and operating points above PVI usually represent the satisfactory operating region [3].

B. VSC-VVO Model Operating in Preventive-Corrective Mode

This subsection explores the situation when multi-timescale VSC-VVO model operates in preventive-corrective mode. Assume initial operating point to be 22.29 MW and -13.8 MVAR with six times increase in constant leading power factor loads. The BESS with capacity of 3.3 MVA/10 MWh, shunt capacitors each with 600 kVAR rating, and PV inverters each with the rating of 1.1 MVA are considered. The tap positions are assumed between 0 and +7. The proposed model maintains 0.92-1.08 pu in normal condition and 0.9-1.1 pu in STE condition.

The VSC-VVO model operation in preventive-corrective mode results in solutions different from standard VVO model. This is due to additional costly preventive measures taken to

1949-3029 (c) 2018 IEEE. Personal use is permitted, but republication/redistribution requires IEEE permission. See http://www.ieee.org/publications_standards/publications/rights/index.html for more information.

This article has been accepted for publication in a future issue of this journal, but has not been fully edited. Content may change prior to final publication. Citation information: DOI 10.1109/TSTE.2019.2910726, IEEE Transactions on Sustainable Energy

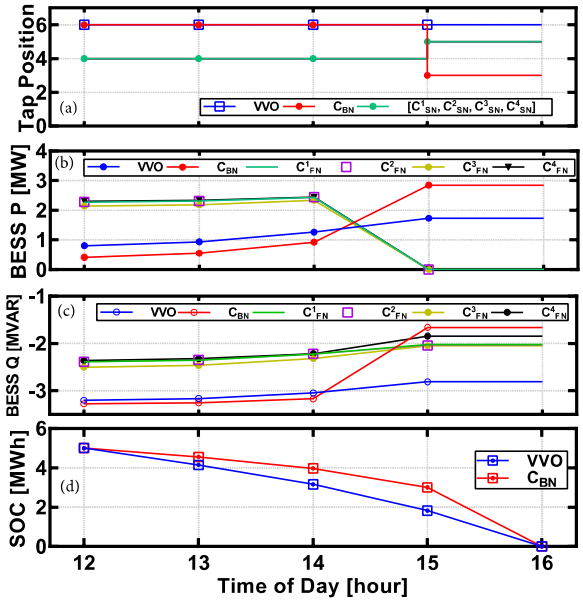

Fig. 14. (a) OLTC tap position. (b) Battery storage active power flow. (c) Battery storage reactive power flow. (d) Battery storage state-of-charge.

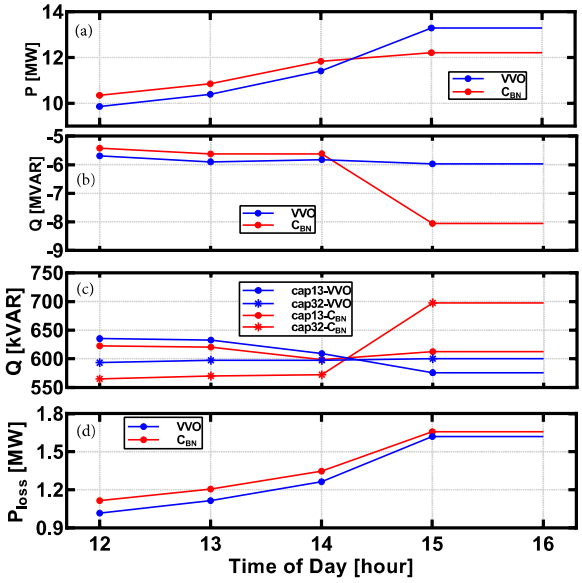

Fig. 15. (a) Substation active power flow. (b) Substation reactive power flow. (c) Shunt capacitors reactive power injections. (d) Distribution losses.

meet the security and stability constraints. Fig. 14(a) shows tap positions and Fig. 14(b) reveals the rising trend of BESS active power injections (case VVO and C_{BN}) with steep rise at instant 15:00 due to high demand and low PV generation. By contrast, the BESS active power becomes zero at instant 15:00 (case C^k) owing to very small post-contingency probabilities. Fig. 14(c) depicts BESS reactive power flows. The BESS with 50% initial state-of-charge is completely discharged to reduce losses and constraint (25c) is not imposed here as indicated by Fig. 14(d).

The preventive measures could move the system away from optimal operating point as evident from Figs. 15 and 16. The substation active and reactive power flows are shown in Figs. 15(a) and 15(b). The capacitor reactive power in Fig. 15(c) is highest at instant 15:00 (case cap32-C_{BN}) due to high voltage magnitude at bus 32. Fig. 15(d) shows the higher power loss in base case C_{BN} as compared to VVO solution.

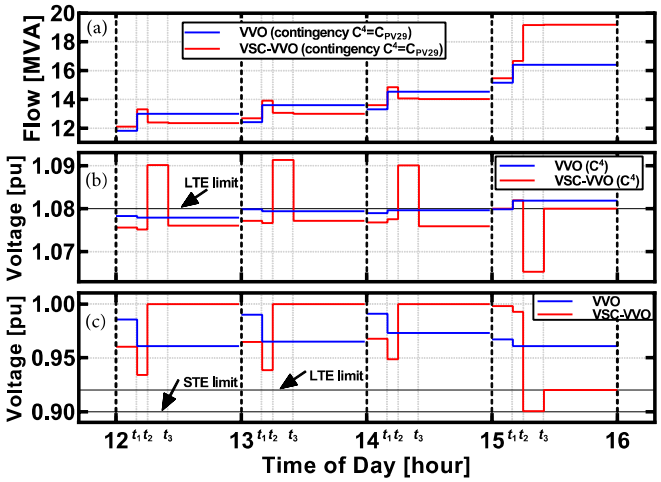

Fig. 16. Simulation. (a) Maximum line flow. (b) Maximum voltage profile. (c) Minimum voltage profile.

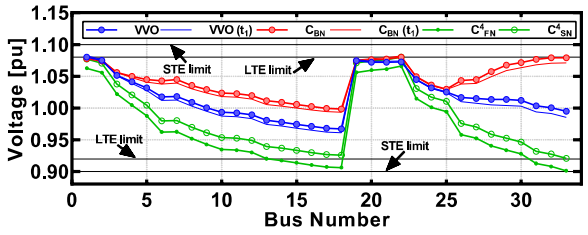

Fig. 17. Feeder voltage profile at instant 15:00.

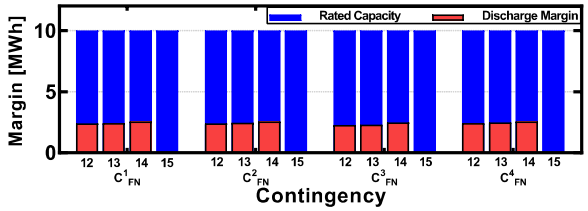

Fig. 18. Battery storage dynamic reserve margin for corrective actions.

The multi-timescale corrective actions exploiting the short-term emergency ratings are shown in Figs. 16 and 17. The line flows are depicted in Fig. 16(a). Fig. 16(b) shows that voltage LTE limit (case VVO) is violated between 15:00-16:00 due to absence of corrective actions in standard VVO model. By contrast, no such violation is observed (case VSC-VVO) because of coordination between fast- and slow-timescale corrective actions. Fig. 16(c) shows that multi-timescale approach exploits the lower STE limit at instant 15:00 (from t_2 to t_3). Fig. 17 shows the entire feeder voltage profile at instant 15:00. The voltages remain within limits and clear rise at profile tail (case C_{BN}) is due to high active power injection from storage.

Fig. 18 demonstrates the coordination between base case state-of-charge and BESS dynamic reserve margin required for post-contingency corrective actions as per (26). The reserve margin is nil at instant 15:00 (case C^k) because the storage discharges completely to reduce base case losses. Fig. 19 shows the P-V curves with $VSM^{(C_{BL})}_{target}$=43% and $VSM^{(C^k)}_{target}$=10%. The voltage stability margin at optimal VVO solution is 40% so VSC-VVO model moves the voltage upward from 0.967 pu to 0.9985 pu to meet 43% target. This preventive operation results in suboptimal solution. The overall losses are 5.0147 MW (VVO) and 5.325 MW (case C_{BN}) indicating 6.18% increase.

The proposed MISOCP model yields global optimum by

1949-3029 (c) 2018 IEEE. Personal use is permitted, but republication/redistribution requires IEEE permission. See http://www.ieee.org/publications_standards/publications/rights/index.html for more information.

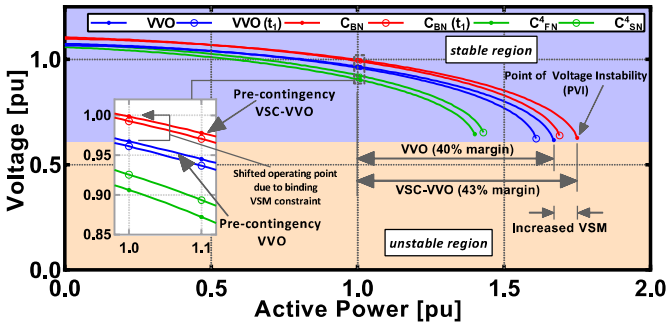

Fig. 19. P-V curves for steady-state voltage stability analysis at instant 15:00.

attaining equality of (28) with zero optimality gap. Figs. 8-19 clearly indicate the feasibility (hence optimality) of solution returned by exact MISOCP relaxation. We have also performed a separate optimization to maximize β subject to fixed control settings using GAMS. The computed point of voltage instability by OpenDSS and GAMS is found to be same indicating the accuracy of results. Simulation times for VVO and VSC-VVO in fully corrective mode are 1.83 s and 444.43 s, respectively.

VI. CONCLUSION

This paper coordinated the post-contingency slow-timescale corrective actions provided by OLTC with fast-timescale corrective actions provided by BESS and PV units. This multi-timescale operation exploited the difference between STE and LTE ratings of line flows and voltage magnitudes. Unlike the standard VVO model, the proposed VSC-VVO model can maintain the voltage stability and security under contingencies. MISOCP model reduced losses and achieved global optimum. Also, the preventive actions are shown to move the stressed system away from global optimum. Proper coordination between base case state-of-charge and storage reserve margin required for post-contingency corrective actions is ensured.

REFERENCES

[1] O. O. Obadina and G. J. Berg, "VAr planning for power system security," *IEEE Trans. Power Syst.*, vol. 4, no. 2, pp. 677–686, May 1989.

[2] B. Cui and X. A. Sun, "A new voltage stability-constrained optimal power flow model: Sufficient condition, SOCP representation, and relaxation," *IEEE Trans. Power Syst.*, pp. 1–1, 2018.

[3] C. W. Taylor, *Power System Voltage Stability*. Singapore: McGraw-Hill Book Co., 1994.

[4] J. Varela, L. J. Puglisi, T. Wiedemann, U. Ysberg, D. Stein, Z. Pokorna, C. Arnoult, R. Garaud-Verdier, and L. Consiglio, "Show me!: Large-scale smart grid demonstrations for European distribution networks," *IEEE Power Energy Mag.*, vol. 13, no. 1, pp. 84–91, Jan. 2015.

[5] H. I. Su and A. E. Gamal, "Modeling and analysis of the role of fast-response energy storage in the smart grid," in *Proc. 49th Annu. Allerton Conf. Commun., Control, and Computing*, Sep. 2011, pp. 719–726.

[6] B. Lu and M. Shahidehpour, "Short-term scheduling of battery in a grid-connected PV/battery system," *IEEE Trans. Power Syst.*, vol. 20, no. 2, pp. 1053–1061, May 2005.

[7] W. Zhang, Y. Xu, Z. Dong, and K. P. Wong, "Robust security constrained-optimal power flow using multiple microgrids for corrective control of power systems under uncertainty," *IEEE Trans. Ind. Informat.*, vol. 13, no. 4, pp. 1704–1713, Aug. 2017.

[8] Y. Wen, C. Guo, and S. Dong, "Coordinated control of distributed and bulk energy storage for alleviation of post-contingency overloads," *Energies*, vol. 7, no. 3, pp. 1599–1620, Mar. 2014.

[9] Y. Wen, C. Guo, D. S. Kirschen, and S. Dong, "Enhanced security-constrained OPF with distributed battery energy storage," *IEEE Trans. Power Syst.*, vol. 30, no. 1, pp. 98–108, Jan. 2015.

[10] J. Cao, W. Du, and H. F. Wang, "An improved corrective security constrained OPF with distributed energy storage," *IEEE Trans. Power Syst.*, vol. 31, no. 2, pp. 1537–1545, Mar. 2016.

[11] W. Zhang, F. Li, and L. M. Tolbert, "Review of reactive power planning: Objectives, constraints, and algorithms," *IEEE Trans. Power Syst.*, vol. 22, no. 4, pp. 2177–2186, Nov. 2007.

[12] D. Chattopadhyay and B. Chakrabarti, "Voltage stability constrained VAR planning: Model simplification using statistical approximation," *Int. J. Elect. Power Energy Syst.*, vol. 23, no. 5, pp. 349 – 358, 2001.

[13] ——, "Reactive power planning incorporating voltage stability," *Int. J. Elect. Power Energy Syst.*, vol. 24, no. 3, pp. 185 – 200, 2002.

[14] J. Liu, Y. Xu, Z. Y. Dong, and K. P. Wong, "Retirement-driven dynamic VAR planning for voltage stability enhancement of power systems with high-level wind power," *IEEE Trans. Power Syst.*, vol. 33, no. 2, pp. 2282–2291, Mar. 2018.

[15] P. Kayal and C. Chanda, "Placement of wind and solar based DGs in distribution system for power loss minimization and voltage stability improvement," *Int. J. Elect. Power Energy Syst.*, vol. 53, pp. 795 – 809, May 2013.

[16] M. Farivar and S. H. Low, "Branch flow model: Relaxations and convexification - Part I," *IEEE Trans. Power Syst.*, vol. 28, no. 3, pp. 2554–2564, Aug. 2013.

[17] J. A. Taylor, *Convex Optimization of Power Systems*. UK: Cambridge University Press, 2015.

[18] R. Madani, M. Ashraphijuo, and J. Lavaei, "Promises of conic relaxation for contingency-constrained optimal power flow problem," *IEEE Trans. Power Syst.*, vol. 31, no. 2, pp. 1297–1307, Mar. 2016.

[19] M. Chamana and B. H. Chowdhury, "Optimal voltage regulation of distribution networks with cascaded voltage regulators in the presence of high PV penetration," *IEEE Trans. Sustain. Energy*, vol. 9, no. 3, pp. 1427–1436, Jul. 2018.

[20] M. Chamana, B. H. Chowdhury, and F. Jahanbakhsh, "Distributed control of voltage regulating devices in the presence of high PV penetration to mitigate ramp-rate issues," *IEEE Trans. Smart Grid*, vol. 9, no. 2, pp. 1086–1095, Mar. 2018.

[21] E. Mohagheghi, A. Gabash, M. Alramlawi, and P. Li, "Real-time optimal power flow with reactive power dispatch of wind stations using a reconciliation algorithm," *Renewable Energy*, vol. 126, pp. 509 – 523, Oct. 2018.

[22] R. Zafar, J. Ravishankar, J. E. Fletcher, and H. R. Pota, "Multi-timescale model predictive control of battery energy storage system using conic relaxation in smart distribution grids," *IEEE Trans. Power Syst.*, vol. 33, no. 6, pp. 7152–7161, Nov. 2018.

[23] E. Mohagheghi, M. Alramlawi, A. Gabash, and P. Li, "A survey of real-time optimal power flow," *Energies*, vol. 11, no. 11, Nov. 2018.

[24] M. Glavic, D. Novosel, E. Heredia, D. Kosterev, A. Salazar, F. Habibi-Ashrafi, and M. Donnelly, "See it fast to keep calm: Real-time voltage control under stressed conditions," *IEEE Power Energy Mag.*, vol. 10, no. 4, pp. 43–55, Jul. 2012.

[25] R. Zafar, J. Ravishankar, and H. R. Pota, "Centralized control of step voltage regulators and energy storage system under high photovoltaic penetration," in *Proc. IEEE Innov. Smart Grid Technol.- Asia*, Nov. 2016, pp. 511–516.

[26] Z. Ziadi, S. Taira, M. Oshiro, and T. Funabashi, "Optimal power scheduling for smart grids considering controllable loads and high penetration of photovoltaic generation," *IEEE Trans. Smart Grid*, vol. 5, no. 5, pp. 2350–2359, Sep. 2014.

[27] L. H. Macedo, J. F. Franco, M. J. Rider, and R. Romero, "Optimal operation of distribution networks considering energy storage devices," *IEEE Trans. Smart Grid*, vol. 6, no. 6, pp. 2825–2836, Nov. 2015.

[28] B. Zhang, A. Y. S. Lam, A. D. Domínguez-García, and D. Tse, "An optimal and distributed method for voltage regulation in power distribution systems," *IEEE Trans. Power Syst.*, vol. 30, pp. 1714–1726, Jul. 2015.

[29] M. Farivar, R. Neal, C. Clarke, and S. Low, "Optimal inverter VAR control in distribution systems with high PV penetration," in *Proc. IEEE Power Energy Soc. Gen. Meeting*, Jul. 2012, pp. 1–7.

[30] I. M. Dudurych, A. Rogers, R. Aherne, L. Wang, F. Howell, and X. Lin, "Safety in numbers: Online security analysis of power grids with high wind pentration," *IEEE Power Energy Mag.*, vol. 10, no. 2, pp. 62–70, Mar. 2012.

[31] (Dec. 2016) Western Power Technical Rules. [Online]. Available: https://westernpower.com.au/media/2312/technical-rules-20161201.pdf

[32] Y. Li, "Decision making under uncertainty in power system using Benders decomposition," Ph.D. dissertation, Iowa State University, 2008.

[33] W. Wu, Z. Tian, and B. Zhang, "An exact linearization method for OLTC of transformer in branch flow model," *IEEE Trans. Power Syst.*, vol. 32, no. 3, pp. 2475–2476, May 2017.

[34] M. E. Baran and F. F. Wu, "Network reconfiguration in distribution systems for loss reduction and load balancing," *IEEE Trans. Power Del.*, vol. 4, no. 2, pp. 1401–1407, Apr. 1989.

[35] J. Sell. (2017) Meeting minutes - IEEE Volt/VAR Task Force. [Online]. Available: http://grouper.ieee.org/groups/td/dist/da/vvtf.html

[36] R. W. Uluski, "Interactions between AMI and distribution management system for efficiency/reliability improvement at a typical utility," in *Proc. IEEE Power Energy Soc. Gen. Meeting*, Jul. 2008, pp. 1–4.

[37] T. Andreas, A.; Stoffel. NREL Solar Radiation Research Laboratory (SRRL): Baseline Measurement System (BMS); Golden, Colorado (Data); NREL Report No. DA-5500-56488. [Online]. Available: http://dx.doi.org/10.5439/1052221

[38] Dynamic load profiles. Southern California Edison. [Online]. Available: https://www.sce.com/nrc/RO/005_regul_info/eca/DOMSM18.DLP

[39] F. Bouffard, F. D. Galiana, and A. J. Conejo, "Market-clearing with stochastic security-Part I: Formulation," *IEEE Trans. Power Syst.*, vol. 20, no. 4, pp. 1818–1826, Nov. 2005.

[40] GAMS/CPLEX. [Online]. Available: https://www.gams.com/latest/docs/S_CPLEX.html

1949-3029 (c) 2018 IEEE. Personal use is permitted, but republication/redistribution requires IEEE permission. See http://www.ieee.org/publications_standards/publications/rights/index.html for more information.